Journal of The Electrochemical Society, **162** (10) A1935-A1939 (2015)
0013-4651/2015/162(10)/A1935/5/$33.00 © The Electrochemical Society

In Situ XAFS Study of the Capacity Fading Mechanisms in ZnO Anodes for Lithium-Ion Batteries

Christopher J. Pelliccione,[a,b,z] Yujia Ding,[a,*] Elena V. Timofeeva,[b] and Carlo U. Segre[a,]**

[a]*Department of Physics & CSRRI, Illinois Institute of Technology, Chicago, Illinois 60616, USA*
[b]*Energy Systems Division, Argonne National Laboratory, Argonne 60439, Illinois, USA*

Correlation of electrochemical performance and in situ X-ray absorption fine structure (XAFS) spectroscopy measurements on ZnO anodes for lithium-ion batteries has enabled a detailed examination of the capacity fading mechanisms in this material. ZnO electrodes were galvanostatically charged/discharged in situ for several cycles while XAFS spectra at the Zn K-edge were taken. X-ray absorption near edge structure (XANES) spectroscopy provided information on the oxidation state of Zn atoms in each charged and discharged state. Modeling of extended X-ray absorption fine structure (EXAFS) provided detailed information on the Zn–O, Zn–Zn and even Zn–Li coordination numbers and atomic distances for each charged and discharged electrode states. Based on the changes in atomic arrangement deduced from EXAFS fitting results, it is suggested that metallic Zn nanoparticles larger than 10 nm in diameter and bulk-like properties are created during the first few cycles. In the first discharged state, a small fraction of metallic Zn is oxidized back to ZnO, but such re-oxidation is only observed in the first discharged state. On subsequent cycling, the local Zn environment is unchanged, indicating that majority of zinc is no longer participating in any electrochemical reaction. The observed rapid capacity fade is correlated to the irreversible conversion of ZnO to metallic Zn and segregation of Zn atoms into the large metallic zinc nanoparticles during the first charge, which is essentially conversion of the high capacity ZnO electrode to a poorly performing metallic Zn anode.

Manuscript submitted April 23, 2015; revised manuscript received June 22, 2015. Published July 11, 2015.

Lithium-ion batteries (LIBs) are the primary power source for portable electronic applications. Graphite is the most common anode material in commercially available products due to its excellent cycle life and specific capacity (theoretical capacity of 372 mAh g^{-1}).[1,2] However, for LIBs to be viable options for large scale applications such as electric vehicles, significant improvements in energy and power densities, along with cycle life of next generation LIBs are needed. Metal oxides are often discussed as reasonable alternatives to traditional carbon anode materials as they exhibit theoretical capacities upwards of three times higher than graphitic anodes.[3–5] ZnO is one of the potential alternatives as it has a theoretical capacity of 978 mAh g^{-1},[3] however it has been reported to suffer from severe capacity loss in the first few cycles, even at slow charging rates.[6–11] Attempts have been made to control the capacity fading by using nano-scale ZnO particles,[3,12–14] coating of ZnO with carbon,[15] nickel,[16] copper,[17] tin,[10,18] and even replacing oxygen with nitrogen[5] and phosphorous[19,20] resulting in modest improvements. In order to successfully stabilize cycling behavior of ZnO the overall lithation/delithiation mechanism must be understood at the atomic level to properly engineer better performing anodes. The proposed reduction-oxidation reactions are[4,5,9]

$$ZnO + 2Li^+ + 2e^- \leftrightarrow Zn + Li_2O \quad [1]$$

$$Zn + Li^+ + e^- \leftrightarrow LiZn \quad [2]$$

where ZnO is converted to Zn and Li_2O on initial charging and, upon further charging, Li directly interacts with the newly formed metallic Zn clusters. Previous transmission electron microscopy studies of other oxide-based anode materials confirm formation of metallic particles embedded within the Li_2O matrix upon the first charge.[21,22] In an effort to understand the lithiation/delithiation mechanism, Fu et al.[4] conducted an ex situ X-ray diffraction (XRD) study on ZnO and observed full conversion to crystalline LiZn phase in fully lithated samples. However, the authors observed more than one Li per Zn participating in the reaction after the first cycle, suggesting some reversibility of Li_2O formation back to ZnO in Equation 1. Irreversible reduction of ZnO to metallic Zn results in a loss of over 2/3 of the theoretical capacity of the starting material with a remaining capacity of only 328 mAh/g once the material begins to directly lithiate the metallic Zn (Eq. 2). Therefore it is of high importance to understand why the conversion to Li_2O is irreversible and propose potential ways to make this process more reversible.[3,5,10,12]

The mechanism of lithium insertion and overall capacity fading in anode materials is a complex combination of both amorphous and crystalline phases that XRD study along cannot adequately measure. X-ray absorption fine structure (XAFS) spectroscopy is an element specific technique which allows the local electronic and atomic environment around only elements of interest to be probed. As XAFS measurements are not dependent on samples to have long range crystalline order, information on any and all crystalline and amorphous phases are accounted for, making it a valuable resource for battery material characterization. XAFS spectra contain two main regions, X-ray absorption near edge structure (XANES) and extended X-ray absorption fine structure (EXAFS) that are sensitive to local electronic information (i.e. oxidation state) and atomic structural information (coordination number, atomic identity and atomic distance) respectively. The EXAFS region can be modeled with theoretical structural models to extract details on the changes occurring at an atomic level.

In this study we use in situ XAFS measurements to study lithiation and delithiation of ZnO anodes during electrochemical cycling. The EXAFS spectra in charged and discharged states are modeled to extract quantitative structural changes around zinc atoms, while the XANES region provides electronic structural information to support the overall model. Based on the atomic model derived from the XAFS results we propose two possible mechanisms for capacity fade. Our results are consistent with previously reported studies,[4,5,9] however the detailed EXAFS modeling supported by XANES results provide a heretofore unavailable interpretation of atomic changes which directly correlate with the observed electrochemical capacity fading.

Experimental

Electrochemical characterization.— ZnO powders (Fisher Scientific; 1314-13-2) were used as active anode material studied against Li metal foil counter electrode in coin cell and pouch cell configurations. Scanning electron microscopy images (Hitachi S-4700) and XRD measurements (Bruker D2 diffractometer), as shown in Figures 1 and 2 in the Supplementary Material, confirm polydisperse particle sizes of ca. 1 μm and $P6_3mc$ ZnO crystal structure.[23] Electrodes were prepared using 80:10:10 wt% of ZnO, acetylene carbon black (STREM Chemicals; 138-86-4), and poly(vinylidene fluoride) binder (Aldrich; 24937-79-9) respectively dispersed in n-methyl-2-pyrrolidinone (Aldrich; 872-50-4) to create a slurry for casting. After sonication and mechanical mixing (ca. 2 hours), the slurry was

*Electrochemical Society Student Member.
**Electrochemical Society Active Member.
zE-mail: cpellic1@hawk.iit.edu

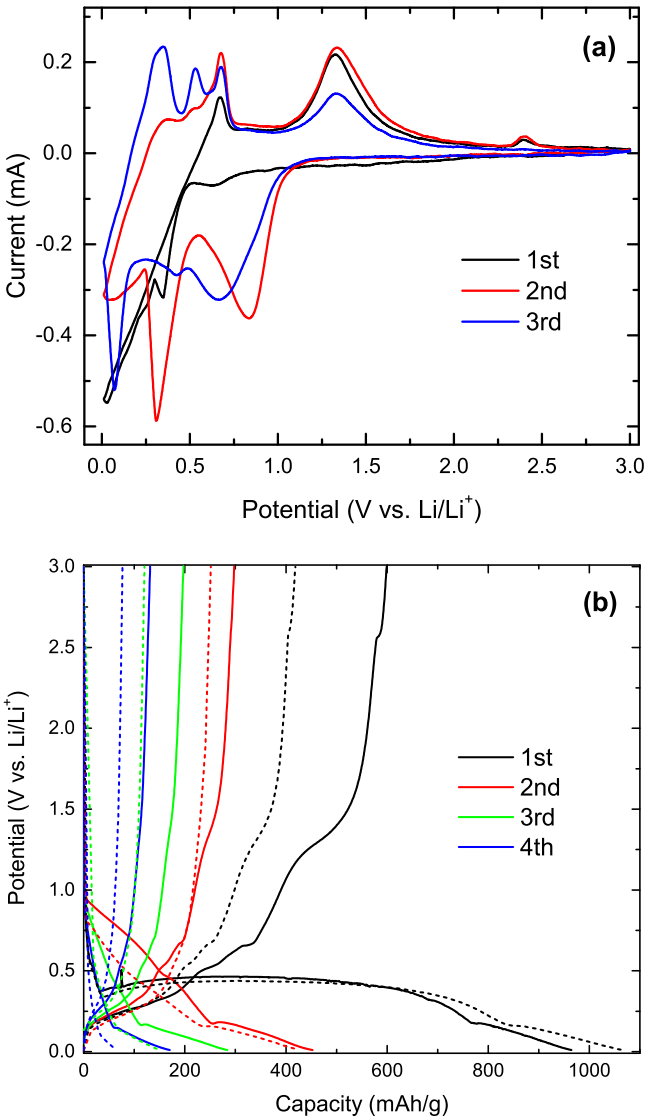

Figure 1. (a) First (black), second (red), and third (blue) CV curves acquired at 0.1 mV/s between 0.01 and 3.00 V vs. Li/Li^+ and (b) coin cell C/10 (solid lines) and in situ C/4 (dashed lines) capacity curves for first (black), second (red), third (green) and fourth (blue) cycles.

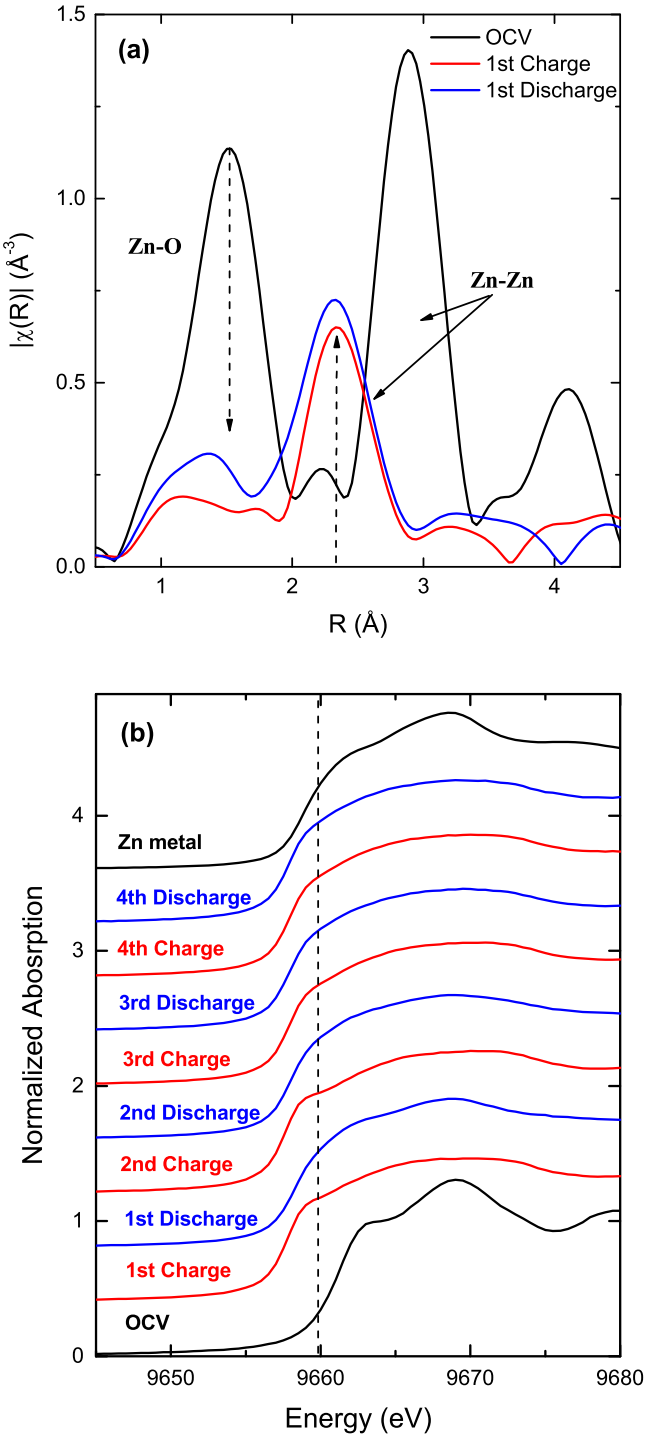

Figure 2. (a) $|\chi(R)|$ plots of pristine ZnO at OCV (black), first charge (red) and first discharge (blue) EXAFS spectra. Dashed arrows emphasizes both the Zn–O and Zn–Zn structural changes from cycle to cycle. (b) XANES spectra of pristine ZnO at OCV and first through fourth cycles for both charged (red) and discharged (blue) states.

deposited on ca. 0.03 mm thick copper foil using a doctor blade and dried on a hot plate set to 100°C for ca. one hour. Electrodes were cut into 1.11 cm diameter disks and coin cells were assembled using 1.59 cm diameter Celgard 2325 separator, and 1.42 cm diameter Li metal foil (0.2 mm thick) with 1M $LiPF_6$ electrolyte (Tomiyama Pure Chemical Industries, LTD; LIPASTE A49). The standard coin cell was crimped using MSK-160D electronic crimper (MTI Corporation). Pouch cells were assembled via stacking active electrode, electrolyte soaked separator, and Li metal foil between metal strips acting as current collectors. All components were placed and sealed within a polyethylene pouch material using a thermal impulse sealer. The pouch cell was then clamped between two plastic plates, applying pressure to ensure good contact throughout the stacked components. Both coin cells and pouch cells were assembled within an inert Ar atmosphere glove box (VAC). Electrochemical characterization was conducted using an EzStat Pro potentiostat/galvanostat (Nuvant Systems Inc.) and BST8-MA battery cycler system (MTI Corporation). Cyclic voltammetry (CV) curves were measured at 0.1 mV/s scan rate between potential limits of 0.01 and 3.00 V vs. Li/Li^+. Galvanostatic charge/discharge curves were measured in a coin cell at C/10 (98 mA g^{-1}, assuming a theoretical capacity of 978 mAh g^{-1}), and in a pouch cell for in situ experiments at C/4 (245 mA g^{-1}).

X-ray absorption fine structure spectroscopy.— In situ XAFS spectra were acquired at the Materials Research Collaborative Access Team (MRCAT) beamline, Sector 10-BM-B, of the Advanced Photon Source at Argonne National Laboratory, IL. A pouch cell was

assembled and secured within a specially designed in situ sample chamber to properly apply pressure on the pouch cell which also provides an inert He atmosphere during data acquisition. Details of the in situ sample chamber and assembly are provided elsewhere.[24] XAFS spectra were collected at the Zn K-edge (9.66 keV) in fluorescence mode using a Vortex-ME4 silicon drift detector (Hitachi High-Technologies Science America, Inc.). The in situ sample chamber was placed at a 45° angle while the fluorescence detector was placed perpendicular to the incident X-ray beam path. Measurements were taken at open circuit voltage (OCV) for the pristine electrode deposition, then for the charged state (0.01 V vs. Li/Li^+), followed by the discharged state (3.00 V vs. Li/Li^+) and repeated for four charge/discharge cycles with the potential being held constant at each state to acquire several scans (ca. 1 hour 30 minutes).

For each charged or discharged state multiple scans were aligned, merged, and normalized using Athena.[25,26] The built in AUTOBK algorithm was used to minimize background below $R_{bkg} = 1.0$ Å. The combined scans for each charge or discharge state were modeled using Artemis with theoretical models created by FEFF6.[25,26] The OCV state was fit using the $P6_3mc$ ZnO structure,[23] as confirmed through XRD (Fig. 2 in the Supplemental Information). The remaining spectra were fit using a LiZn structure[27] with the exception of the first discharged state spectrum which was fit using a combination of the metallic Zn crystal structure[28] and a Zn–O path. Initially a Zn–O path was included in each charged and discharged state model, but a statistically significant contribution from this path was observed only in the first discharged state spectrum. All spectra were fit simultaneously in k, k^2 and k^3 weighting using a Hanning window from 2.0–9.5 $Å^{-1}$. The R–range for all fits were 1.2–3.0 Å, with the exception of the OCV state which was fit from 1.0–3.6 Å to fully include the contribution of the next-near neighbor Zn atoms.

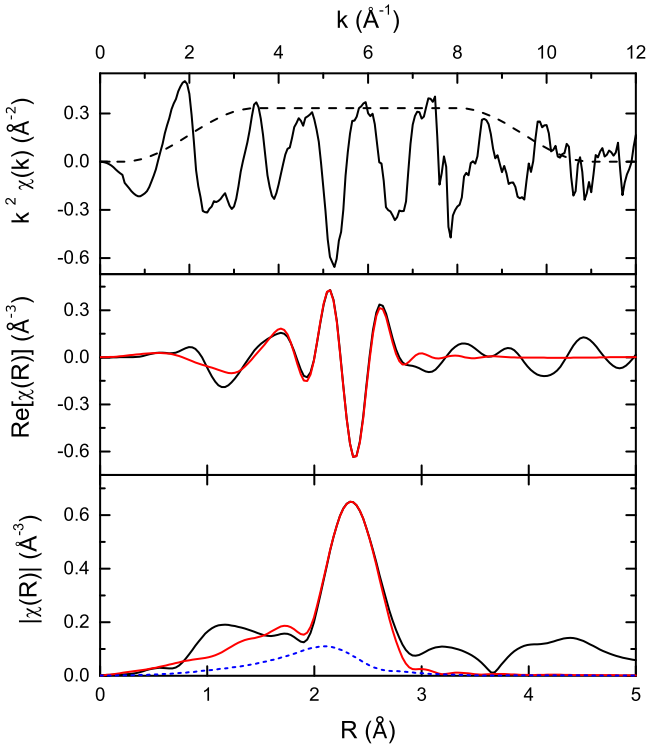

Figure 3. $k^2\chi(k)$, $Re[\chi(R)]$ and $|\chi(R)|$ plots for first charged EXAFS spectrum. The black line represents the data, red line is the corresponding fit and blue dashed line shows the Zn–Li contribution to the $|\chi(R)|$ fit. The Fourier transform window in k–space is shown in the top panel.

Results and Discussion

Prior to the in situ XAFS experiment, ZnO electrodes were studied via cyclic voltammetry in pouch cells. Evolution of initial CV curves is shown in Figure 1a with anodic peaks located at 0.85 V, 0.42 V and 0.06 V while upon cathodic sweeps peaks develop by the third cycle at 0.33 V, 0.55 V, 0.68 V, and 1.32 V along with a minor peak at 2.40 V that completely disappears by the third cycle. It has been discussed in previous work[12,16] that the majority of the peaks developed by the third CV cycle correspond to various Li–Zn phases. The large anodic peak at 0.06 V observed on the first cycle is a combination of oxygen conversion to Li_2O and lithium insertion. The peak at 2.40 V has previously been prescribed to a slight re–oxidation of metallic Zn back to ZnO.

Figure 1b displays the first four charge/discharge capacity curves for coin cell and in situ pouch cell measurements. The first discharge curve in both coin cell and in situ experiments exhibit a small plateau at ca. 2.50 V, which similarly to the CV curves, disappears in subsequent charge/discharge cycles. An initial discharge capacity in a coin cell is ca. 600 $mAhg^{-1}$, and in just four cycles it reduces by 78% to 170 mAh g^{-1}. The freshly prepared pouch cell, measured within the in situ sample chamber, exhibits an initial discharge capacity of ca. 420 mAh g^{-1} with reduction of 82% by the fourth cycle. This type of dramatic capacity fading is similar to results presented in previous studies.[12,13] Reduced electrochemical performance seen in the in situ pouch cell compared to the coin cell is expected due to the faster charge/discharge rates and also due to limitations presented by in situ XAFS experiments, specifically the reduced ability to apply pressure to pouch cells within the in situ sample chamber without significantly degrading the X-ray signal.[24]

Figure 2 shows both R-space (Fourier transform of the $\chi(k)$) and XANES results. In R-space, large changes occur between pristine ZnO at OCV and the first charged state as the intensity of the Zn–O peak is greatly reduced, and the Zn–Zn distance decreases from 3.25 $\pm$ 0.01 Å at OCV to 2.64 $\pm$ 0.01 Å in the first charged state (distances displayed in Figure 2a are not corrected for appropriate phase shifts). The latter distance is typical for metallic Zn. In the first discharged state, a slight variation occurs in the Zn–Zn peak, particularly a change in the 'shoulder' at shorter distances. The XANES (Fig. 2b) also show significant changes from OCV to the first charged state as the edge position shifts to lower energy, which is a slightly lower energy than that for metallic Zn (denoted by vertical dashed line in Fig. 2b). This suggests all of ZnO converts to metallic Zn, and a fraction of this newly formed metallic Zn further converts to a Zn^- state (i.e. LiZn formation). In the first discharged state, the edge position shifts to a primarily metallic Zn position. In the second charged state the edge is shifted back to a position similar to the first charged state, however subsequent cycling shows minimal changes, and by the fourth charge/discharge cycle the edge position remains static at an energy similar to that observed in the first charged state.

Initial fits for all EXAFS spectra used a simple model of Zn–O and metallic Zn (except for the pristine electrode at OCV which used the ZnO structure[23]). However this approach did not provide satisfactory fits in most states, particularly at the lower k and k^2 weightings indicating the model was missing a significant light–element contribution. Zn–Li paths were included where necessary, replacing the metallic Zn model with the LiZn structure[27] which has four Zn–Li and four Zn–Zn near neighbors both with bond distances of 2.70 Å . The inclusion of the Zn–Li contribution greatly improved the fits in all k weightings. The Zn–Li distance was determined from fitting the first charged state (2.66 $\pm$ 0.01 Å) and was set for all other fits that required Zn–Li paths. In addition, the Zn-O path was removed from the model for fits in which there was no statistically significant Zn–O contributions (all except the pristine ZnO electrode at OCV and the first discharged state). An example fit is shown in Figure 3 in $k^2\chi(k)$, $Re[|\chi(R)|]$, and $|\chi(R)|$ plots for the first charged state. The Zn–Li path is also shown to illustrate it's significance to the model. Fits and detailed results for all charged and discharged states are shown in Figure 3 in the Supplemental Information.

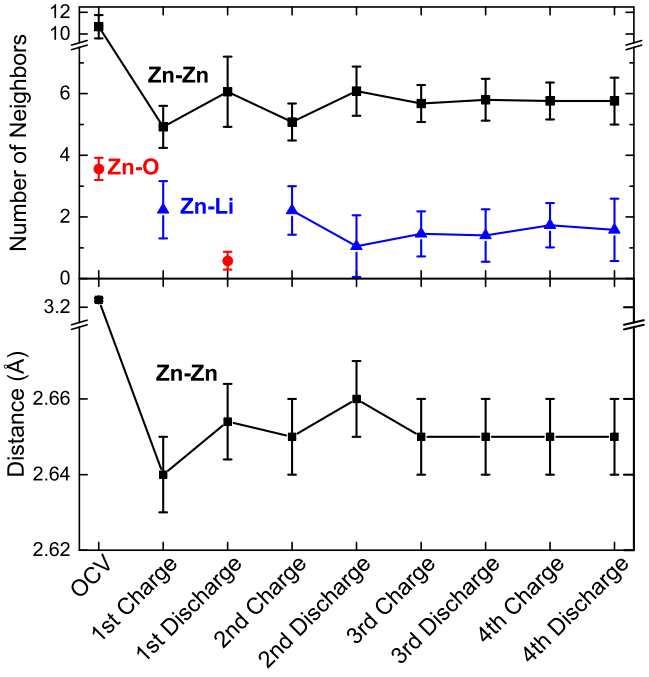

Figure 4. (Top) number of near neighbors for Zn–Zn, Zn–O and Zn–Li and (bottom) corresponding interatomic distance as a function of charge/discharge state determined from fitting EXAFS spectra. Zn–Li distances have been excluded from the top graph as they were all set to 2.66 ± 0.01 Å, as determined from the fit of the first charged state.

The EXAFS fitting results of Zn–Zn atomic distance and the number of near neighbors for Zn–Zn, Zn–O and Zn–Li as a function of the cycle number and charge state are presented in Figure 4. The number of Zn–O near neighbors decreases from 3.56 ± 0.36 in the pristine OCV state to nearly zero in the first charged state. Conversion of ZnO to Zn is mostly irreversible, minor amounts of ZnO reappear in the first discharged state with 0.6 ± 0.3 near neighbors at a distance of 1.93 ± 0.03 Å, which is a contraction of ca. 0.05 Å from the pristine Zn–O interatomic distance. The contribution of Zn–O fully disappears in the subsequent cycled states which correlates to the small plateau at ca. 2.50 V in the capacity curves that is also only observed in the first discharge curve (Fig. 1b). The latter confirms that the transition at 2.50 V is due to the partial oxidation of metallic Zn in the first charged state to ZnO during the first discharge.

The Zn–Zn coordination number decreases from 10.7 ± 1.1 at OCV to 4.9 ± 0.7 near neighbors at in the first charged state with a drastic shortening of the distances as mentioned earlier. In addition to the change in Zn–Zn environment, a Zn–Li path emerges in the first charged state with 2.2 ± 0.9 near neighbors, which is lower than the expected four near neighbors dictated by the LiZn crystal structure. This implies that in a fully charged state, there is an incomplete conversion of metallic Zn to LiZn, suggesting that the metallic Zn phase is still present.

Upon the first discharge, all statistically significant Zn–Li neighbors disappear and the number of Zn–Zn neighbors are increased to 6.1 ± 1.0, suggesting a primarily metallic Zn environment (six Zn–Zn near neighbors at 2.64 Å). Zn–Li contributions return in the second charged state with 2.2 ± 0.8 neighbors. In the second discharged state, Zn–Li neighbors are not fully removed with 1.1 ± 1.0 near neighbors remaining. This is in agreement with the decrease in electrochemical performance on the second charge/discharge cycle (Fig. 1b) with ca. 46% drop in capacity from first discharged state. The latter suggests that the Li inserted upon charging is not fully removed on discharge. The third and fourth cycles show almost no change in either the near neighbor or distance in any of the Zn–Zn, Zn–O or Zn–Li paths, meaning the Zn local environment is no longer participating in any lithiation/delithiation process.

The degradation of ZnO seems to be most severe within the first two or three cycles and involves a large structural change from the pristine ZnO structure at OCV to the first charged state, as suggested by Eqs. 1 and 2. Specifically, EXAFS data indicate that atomic clusters of metallic Zn are formed when oxygen is converted to Li_2O. Based on the number of Zn–Zn near neighbors (6.1 ± 1.0) and the atomic distance (2.64 ± 0.01 Å), which are within fitting error of the bulk metallic Zn structure (six near neighbors at 2.64 Å), the size of the clusters is suggested to be fairly large (ca. 10 – 20 nm). Once the mostly metallic Zn dominated environment is formed, the electrochemical performance of the electrode quickly declines (Fig. 1b). Emergence of Zn–Li near neighbors, along with observed XANES shifts, indicate that a LiZn phase is formed in fully charged states. Upon the first discharge, all Li atoms are removed from LiZn and a small percentage of Zn is oxidized back to some ZnO phase. The fraction of metal participating in the re-oxidation is small most likely because when metallic Zn clusters are formed, only the 'surface' of these clusters are in close enough proximity to any lingering oxygen or Li_2O to participate. Subsequent charging is then dominated by Li interacting directly with these metallic Zn particles.

From the described EXAFS model, two mechanisms can be proposed that explain severe capacitive decline in ZnO anodes. The first mechanism is based on the growing size of Zn particles within the Li_2O matrix during charge/discharge cycles. When the Zn particles are large enough to behave as bulk metallic Zn, they undergo expansive cracking and fracturing, resulting in loss of electrical contact during charge/discharge cycles.[19] This is supported by the EXAFS results, as after the second discharge, there is a significant amount of residual Li remaining (1.1 ± 1.0 near neighbors) indicating loss of electrical contact has started. Although it is has been confirmed in electron microscopy studies other metal oxide anodes,[21,22,29] the formation of Li_2O is not directly visible using EXAFS but can be deduced from changes in the local environment of Zn atoms. It is clear from our results that the oxygen is removed from proximity of the Zn atoms, creating metallic Zn particles with either Li_2O or some other form of decomposition products separating them. For simplicity, we will refer to this separating layer as Li_2O. Further cycling shows no significant atomic or electronic structural changes occurring, consistent with the very low capacities exhibited by this anode material after the initial cycles.

A second possible mechanism is also related to the segregation of Zn atoms into large clusters during the first several cycles. However the loss of electrochemical activity comes not from fracturing of Zn particles, but from the thickness of the Li_2O layers between the nanoparticles, which also grows as Zn atoms segregate. When the Li_2O layers may reach some critical thickness, the electrical conductivity of the system can be dramatically reduced and result in poor electrochemical performance, as only a small fraction of active material participates in the charge/discharge process.

This EXAFS study is not able to differentiate between these two scenarios both based on the loss of electrical contact of active material. In one the decline in capacity results directly from the degradation of the metallic Zn crystal structure and in the other it is due to the thickening of the Li_2O network separating metallic Zn clusters. Further studies such as in situ TEM, in which the formation of metallic Zn particles can be carefully observed can provide results to further clarify the mechanism of metallic Zn cluster growth.

Conclusions

Analysis of XAFS spectra measured in situ from charged and discharged states of ZnO electrodes provides unique insight into the complex mechanism of Li interactions with Zn based anode materials. The changes in the local atomic environment around Zn atoms indicate segregation of Zn atoms into the large nanoparticles and

removal of oxygen from the proximity of Zn atoms. Interpretation of observed changes suggest two possible mechanisms resulting in rapid electrochemical capacity fade. In agreement with previous studies,[4,5,9] upon first charge zinc oxide is converted to Li_2O and metallic Zn as observed in the change in Zn–O local environment (Fig. 4). The newly formed metallic Zn species partially evolve into a LiZn structure when fully charged. Upon the first discharge, we directly observe a slight re-oxidation of Zn to ZnO as suggested by Fu et al.[4] that is only present in the first discharged state in addition to the remaining bulk-like metallic Zn particles. After the second discharged state, subsequent cycling shows a lack of electronic (Fig. 2b) and atomic (Fig. 4) structural changes. The latter is most likely due to the loss of electrical contact and inability to participate in electrochemical processes. Both proposed mechanisms imply loss of electrical connectivity to the active material within the electrode, with one suggesting fracturing of large Zn particles and the other isolation of metallic Zn particles within thick layers of a Li_2O network. Future studies involve the development of strategies to mitigate segregation of metallic Zn and improve the reversibility of ZnO reduction using the knowledge of the discovered capacity fading mechanisms. Both solutions would improve electrochemical performance of economically attractive Zn-based anodes. In particular, nanoscale morphology, or lack thereof, in anode materials appears to be critical for performance and capacity loss. Additionally, in situ XAS studies on various Zn based compounds with varying crystal structures could indicate less destructive lithation/delithiation mechanisms suggesting new approaches to the development of novel anodes with advanced long term electrochemical performance.

Acknowledgment

C.J.P. was supported by a Department of Education GAANN Fellowship, award #P200A090137. The project is supported by US Department of Energy, Office of Basic Energy Science and Advanced Research Project Agency-Energy (ARPA-E) under Award #AR-000387. MRCAT operations are supported by the Department of Energy and the MRCAT member institutions. Use of the Argonne National Laboratory Advanced Photon Source and Electron Microscopy Center are supported by the U.S. Department of Energy, under Contract No. DE-AC02-06CH113

Supplementary Material.— SEM images of pristine ZnO powder along with comparison XRD of studied ZnO powder and ZnO standard are shown. In addition, all EXAFS fits in $k^2\chi(k)$, $Re[\chi(R)]$ and $|\chi(R)|$ are shown along with a table of detailed fitting results.

References

1. T. Zheng, J. N. Reimers, and J. R. Dahn, *Phys. Rev. B: Condens. Matter Mater. Phys.*, **51**, 734 (1995).
2. Y. F. Reynier, R. Yazami, and B. Fultz, *J. Electrochem. Soc.*, **151**, A422 (2004).
3. X. H. Huang, X. H. Xia, Y. F. Yuan, and F. Zhou, *Electrochim. Acta*, **56**, 4960 (2011).
4. Z. W. Fu, F. Huang, Y. Zhang, Y. Chu, and Q. Z. Qin, *J. Electrochem. Soc.*, **150**, A714 (2003).
5. N. Pereira, L. C. Klein, and G. G. Amatucci, *J. Electrochem. Soc.*, **149**, A262 (2002).
6. J. Liu, Y. Li, R. Ding, J. Jiang, Y. Hu, X. Ji, Q. Chi, Z. Zhu, and X. Huang, *J. Phys. Chem. C*, **113**, 5336 (2009).
7. M. Ahmad, S. Yingying, A. Nisar, H. Sun, W. Shen, M. Wei, and J. Zhu, *J. Mater. Chem.*, **21**, 7723, (2011).
8. J. Liu, Y. Li, X. Huang, G. Li, and Z. Li, *Adv. Funct. Mater.*, **18**, 1448 (2008).
9. M. P. Bichat, J. L. Pascal, F. Gillot, and F. Favier, *Chem. Mater.*, **17**, 6761 (2005).
10. F. Belliard and J. T. S. Irvine, *J. Power Sources*, **97–98**, 219 (2001).
11. Z. Shi, M. Liu, and J. L. Gole, *Electrochem. Solid–State Lett.*, **3**, 312 (2000).
12. H. Wang, Q. Pan, Y. Cheng, J. Zhao, and G. Yin, *Electrochim. Acta*, **54**, 2851 (2009).
13. W. T. Song, J. Xie, S. Y. Liu, Y. X. Zheng, G. S. Cao, T. J. Zhu, and X. B. Zhao, *Int. J. Electrochem. Sci.*, **7**, 2164 (2012).
14. J. Wang, G. Wang, L. Yang, S. H. Ng, and H. Liu, *J. Solid State Electrochem.*, **10**, 250 (2006).
15. M. Yu, A. Wang, Y. Wang, C. Li, and G. Shi, *Nanoscale*, **6**, 10746 (2014).
16. C. Q. Zhang, J. P. Tu, Y. F. Yuan, X. H. Huang, X. T. Chen, and F. Mao, *J. Electrochem. Soc.*, **154**, A65 (2007).
17. L. Wang, S. Kitamura, K. Obata, S. Tanase, and T. Sakai, *J. Power Sources*, **141**, 286 (2005).
18. Y. F. Yuan, J. P. Tu, H. M. Wu, C. Q. Zhang, S. F. Wang, and X. B. Zhao, *J. Power Sources*, **165**, 905 (2007).
19. H. Hwang, M. G. Kim, Y. Kim, S. W. Martin, and J. Cho, *J. Mater. Chem.*, **17**, 3161 (2007).
20. M. S. Kishore and U. V. Varadaraju, *J. Power Sources*, **144**, 204 (2005).
21. P. Poizot, S. Laruelle, S. Grugeon, L. DuPont, and J. M. Tarascon, *Nature*, **407**, 496 (2000).
22. T. Brousse, R. Retoux, U. Herterich, and D. M. Schleich, *J. Electrochem. Soc.*, **145**, 1 (1998).
23. H. Schulz and K. H. Thiemann, *Solid State Commun.*, **32**, 783 (1972).
24. C. J. Pelliccione, E. V. Timofeeva, J. P. Katsoudas, and C. U. Segre, *Rev. Sci. Instrum.*, **27**, 574 (2014).
25. M. Newville, *J. Synchrotron Rad.*, **8**, 322 (2001).
26. B. Ravel and M. Newville, *J. Synchrotron Rad*, **12**, 537 (2005).
27. K. Kuriyama, S. Saito, and K. Iwamura, *J. Phys. Chem. Solids*, **40**, 457 (1979).
28. E. A. Owens, L. Pickup, and J. O. Roberts, *Z. Kristallogr.*, **91**, 70 (1935).
29. Y. J. Kim, M. S. Park, H. J. Sohn, and H. Lee, *J. Alloys Compd.*, **509**, 4367 (2011).